Bioactive Materials 24 (2023) 26–36

Contents lists available at ScienceDirect

Bioactive Materials

journal homepage: www.keaipublishing.com/en/journals/bioactive-materials

Nanoengineered sonosensitive platelets for synergistically augmented sonodynamic tumor therapy by glutamine deprivation and cascading thrombosis

Liqiang Zhou [a], Wei Feng [b], Yuhang Mao [c], Yu Chen [b,*], Xuanjun Zhang [a,**]

[a] MOE Frontiers Science Center for Precision Oncology, Faculty of Health Sciences, University of Macau, Macau, SAR, 999078, China
[b] Materdicine Lab, School of Life Sciences, Shanghai University, Shanghai, 200444, China
[c] School of Medical Technology, Xi'an Medical College, Xi'an, 710021, Shanxi, China

ARTICLE INFO

Keywords:
Sonosensitive platelets
Glutamine deprivation
Sonodynamic tumor therapy
Amino acid starvation
Drug delivery

ABSTRACT

Ultrasound (US)-activated sonodynamic therapy (SDT) stands for a distinct antitumor modality because of its attractive characteristics including intriguing noninvasiveness, desirable safety, and high tissue penetration depth, which, unfortunately, suffers from compromised therapeutic efficacy due to cancer cell-inherent adaptive mechanisms, such as glutathione (GSH) neutralization response to reactive oxygen species (ROS), and glutamine addictive properties of tumors. In this work, we developed a biological sonosensitive platelet (PLT) pharmacytes for favoring US/GSH-responsive combinational therapeutic of glutamine deprivation and augmented SDT. The amino acid transporter SLC6A14 blockade agent α-methyl-$_{DL}$-tryptophan (α-MT)-loaded and MnO_2-coated porphyrinic metal-organic framework (MOF) nanoparticles were encapsulated in the PLTs through the physical adsorption of electrostatic attraction and the intrinsic endocytosis of PLTs. When the sonosensitive PLT pharmacytes reached tumor sites through their natural tendencies to TME, US stimulated the PLTs-loaded porphyrinic MOF to generate ROS, resulting in morphological changes of the PLTs and the release of nanoparticles. Subsequently, intracellular high concentration of GSH and extracellular spatio-temporal controlled US irradiation programmatically triggered the release of α-MT, which enabled the synergistically amplified SDT by inducing amino acid starvation, inhibiting mTOR, and mediating ferroptosis. In addition, US stimulation achieved the targeted activation of PLTs at tumor vascular site, which evolved from circulating PLTs to dendritic PLTs, effectively blocking the blood supply of tumors through thrombus formation, and revealing the encouraging potential to facilitate tumor therapeutics.

1. Introduction

The sustained growth and long-term survival of most cancers mainly rely on high rates of aerobic glycolysis [1], paradoxically, certain cancer cells exhibit 'glutamine addiction' in spite of the actual role of glutamine as a non-essential amino acid (NEAA) [2]. This is not only because of its significant role as a nitrogen donor in protein and nucleotide synthesis [3], but also owing to the critical functions in uptake of essential amino acids (EAA) and maintenance of target of rapamycin (TOR) kinases [4]. Furthermore, as the principal mitochondrial substrate, glutamine potentially contributes to preserving mitochondrial membrane potential (MMP), and holding out the generation of nicotinamide adenine dinucleotide phosphate (NADPH) and glutathione (GSH) required for balancing cellular redox homeostasis [5,6].

Spurred by the strong dependency of cancer cell to glutamine, it is worth considering the possibility of exploiting targeted anticancer therapies by interfering glutamine metabolism. Targeting glutamine addiction by blocking amino acid transporter to suppress glutamine uptake would be a promising cancer therapeutic [7]. SLC6A14, an amino acid transporter with unique characteristics of specifically transporting leucine, glutamine, and arginine, is up-regulated specifically in certain cancer cells, such as estrogen receptor (ER)-positive breast cancer [8], colon cancer [9], and cervical cancer [10] to meet their increased amino acids energy demands in support of exceptionally

Peer review under responsibility of KeAi Communications Co., Ltd.
* Corresponding author.
** Corresponding author.
E-mail addresses: chenyuedu@shu.edu.cn (Y. Chen), xuanjunzhang@um.edu.mo (X. Zhang).

https://doi.org/10.1016/j.bioactmat.2022.11.020
Received 31 August 2022; Received in revised form 6 November 2022; Accepted 27 November 2022

rapid proliferation rate [9]. Mechanically, blockade of SLC6A14 in cancer cells by treatment with a selective blocker could produce a cytostatic effect on the cell growth, and cause apoptotic cell death by inducing amino acid starvation, inhibiting mTOR, and activating autophagy [8].

As a novel generation of hybrid porous nanomaterials, metal-organic framework (MOF) nanostructure has been developed as a desirable nanocarrier for the delivery of therapeutic agents due to its superb loading sites and porous inner structure [11]. After loading the SLC6A14 blockade agent α-methyl-$_{DL}$-tryptophan (α-MT), MOF was further wrapped by the MnO_2 layer to prevent drug leakage and achieve targeted drug release triggered by high GSH levels in the tumor microenvironment (TME) [12]. Moreover, nanosized porphyrin MOF could also serve as sonosensitizers with exceptional sonodynamic therapy (SDT) activity to induce cell apoptosis [13,14]. In particular, in addition to medicating glutamine starvation of cancer cells, the loaded α-MT could also prevent internal GSH synthesis by limiting the entry of external glutamine, thereby cooperatively augmenting the ROS-induced cell killing efficacy [15]. However, the broad nanomedicine applications of metallic nanomaterials are limited by their suboptimal biosecurity and low biocompatibility [16]. Adsorption of nanomaterials onto primitive living cells with different physiological functions through nano-engineering techniques, such as platelet (PLT) cells, can effectively solve this tough challenge owing to their innate tendencies to accumulate at tumor wounds [17], thus presenting the advantages of desirable serum stability, active tumor targeting and prolonged blood circulation [18,19].

In this study, we report the construction of self-adaptive sonosensitive PLT pharmacytes to mediate cascaded delivery of the engineered porphyrinic MOF nanostructure, which were loaded with selective amino acid transporter blocker α-MT and coated with MnO_2 unlocked layer, favoring ultrasound (US)/GSH-responsive combinational therapeutics between glutamine deprivation and SDT (Scheme 1). When the integrated bio-nano platform (designated as αMM@PLT) reached tumor sites through the inherent TME tropism of PLTs, US stimulated the PLTs-loaded porphyrinic MOF to generate ROS, resulting in morphological changes of the PLTs and the release of nanoparticles. Subsequently, the outer MnO_2-coated layer of αMM would be decomposed by the excessive GSH in TME to trigger the release of encapsulated α-MT for blocking the glutamine addition and intervening glutamine metabolism. US stimulation with precise spatio-temporal control could further promote targeted release of therapeutic drugs and simultaneously perform SDT of tumors. Especially, the consumption of intracellular GSH incited by MnO_2 and the lack of raw materials for GSH synthesis induced by α-MT enabled significantly improved sensitivity of tumor SDT. Furthermore, US stimulation mediated the de-extending pseudopodia of circulating PLTs to evolve into dendritic PLTs and form thrombi, effectively blocking the blood supply to the tumor. PLTs-delivered and US/GSH-triggered programmed drug release endued our designed bio-nano platform with no unexpected drug leakage and high drug delivery

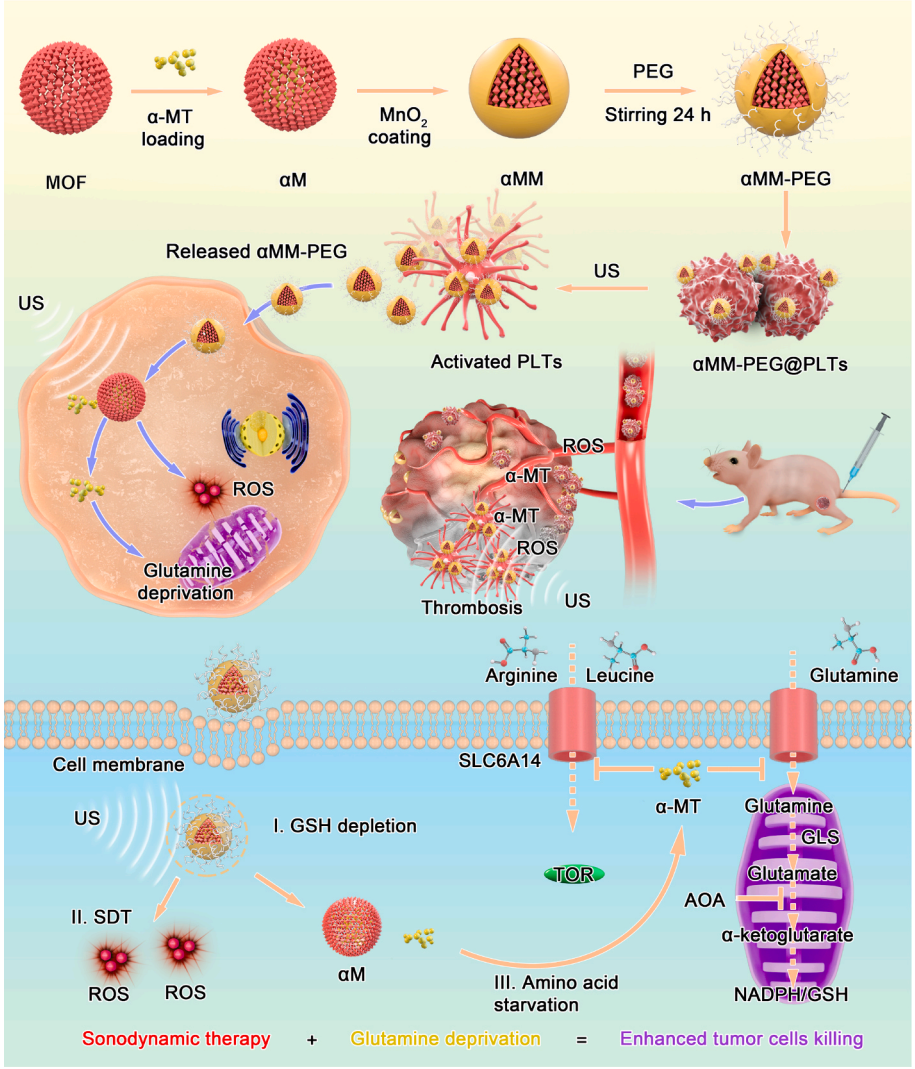

Scheme 1. Schematic illustration of underlying therapeutic mechanism of αMM@PLTs bio-nano platform for synergistically augmented sonodynamic anticancer therapy by stimuli-responsive glutamine deprivation and blood blockade. When the integrated αMM@PLTs bio-nano platform reached tumor sites through natural targeting of circulating platelets, the outer MnO_2 layer of αMM would be decomposed by the excessive GSH in TME to trigger the release of encapsulated α-MT for blocking the amino acid uptake (glutamine, arginine, and leucine) and intervening glutamine metabolism. US stimulation further promoted intratumoral release of therapeutic drugs and simultaneously activated TCPP-mediated SDT. Consequently, the unlocking of endogenous consumption and blocking of exogenous synthesis of GSH enabled significantly augmented sensitivity of SDT. Furthermore, US stimulation mediated the de-extending pseudopodia of circulating PLTs to evolve into dendritic PLTs and form thrombi, effectively blocking the blood supply to the tumor.

efficiency. Consequently, the amplified therapeutic effects of predominate cancer glutamine deprivation, potent SDT and cascading thrombosis would efficiently restrain the cancer growth in a synergistic promotion manner.

2. Materials and methods

Materials and Reagents. Zirconyl chloride octahydrate ($ZrOCl_2{\cdot}8H_2O$), 5,10,15,20-tetrakis (4-carboxyphenyl) porphyrin (H_2TCPP), benzonic acid, DMF, potassium permanganate ($KMnO_4$), and α-methyl-$_{DL}$-tryptophan (α-MT) were purchased from Sigma-Aldrich (Shanghai, China). Materials for cell culture, including Dulbecco's phosphate buffered saline (PBS), Dulbecco's modified Eagle's medium (DMEM), fetal bovine serum (FBS), penicillin-streptomycin, and trypsin, were purchased from Gibco Corporation (Shanghai, China). Cell-counting kit-8 (CCK-8), 2,2,6,6-Tetramethylpiperidine (TEMP), and DAPGreen (D676) autophagy detection probe were purchased from Dojindo Molecular Technologies. 3-Methyladenine (3-MA) was purchased from MedChemExpress. 2′,7′-dichlorofluorescin diacetate (DCFH-DA) was bought from Beyotime Biotechnology. GSH assay kit was purchased from Beyotime Institute of Biotechnology (China). Antirabbit LC3A/B antibody (D3U4C), antirabbit Glutathione Peroxidase 4 antibody (59735), antimouse CHOP (L63F7) antibody (2895T), antirabbit p70 S6 Kinase (49D7) antibody (2708T), antirabbit Phospho-S6 Ribosomal Protein (Ser240/244) (D68F8) antibody (5364T), Cleaved Caspase-3 (Asp175) antibody (9661T), and antirabbit Cleaved PARP (Asp214) antibody (9541T) were purchased from Cell Signaling Technology. Asparagine synthetase (G-10) antibody (sc-365809), and Lamin A antibody (sc-71481) were purchased from SantaCruz.

Synthesis of Zr-Based Porphyrinic MOF. Zr-MOF nanoparticles were optimized synthesized based on previous reported methods [16]. Simply, 100 mg TCPP, 300 mg $ZrOCl_2{\cdot}8H_2O$, and 2.8 mg benzoic acid (BA) were dissolved in 100 mL DMF and stirred at 90 °C for 5 h. After completing the above operations, the obtained mixture was centrifuged at 11 000 rpm for 30 min, and washed thoroughly with DMF 3 times. The obtained Zr-MOF nanoparticles were stored in DMF solution at 4 °C and protected from light.

Synthesis of α-MT@MOF(αM). The as-synthesized 2 mg Zr-based porphyrinic MOF was dispersed in 1 mL deionized water. Then, 2 mg of α-MT was dissolved in 1 mL of dilute hydrochloric acid (0.5 mol L^{-1}), and the pH was adjusted to 7.4 with sodium hydroxide. The dissolved α-MT was added to the dispersion of MOF and magnetically stirred at 25° Celsius for 24 h. The α-MT@MOF (αM) nanoparticles were gathered by constant speed centrifugation at 11 000 rpm for 30 min and washed with deionized water for 3 times to clear away the unattached α-MT.

Synthesis of MnO_2 Coated α-MT@MOF (αMM). For the synthesis of α-MT@MOF@MnO_2, 4 mg α-MT@MOF was suspended in 5 mL deionized water in which 8 mg PAH was dissolved, and the solution was agitated for 4 h at 1000 rpm. Next, 100 μL of 10 mg mL^{-1} $KMnO_4$ aqueous solution was slowly added dropwise to the above mixed solution, and agitated for 2 h at 1000 rpm. When the solution color altered from purple to yellow-brown, it indicated the successful synthesis of MnO_2-coated MOF.

Cell Culture and Animals. a) Cell culture. The human ZR-75-1 cells were cultured in RPMI-1640 complete culture medium in a 37° Celsius incubator supplied with a humidified atmosphere of 5% CO_2. b) Animals. 40 6-week-old female BALB/c nude mice were obtained from Shanghai Experimental Animal Center (Shanghai, China). All animal experiments were performed in accordance with relevant animal care guidelines and were approved by the Ethics Committee of Shanghai University.

Platelet Collection. Blood was drawn from the mouse orbital sinus and collected into centrifuge tubes containing citrate dextrose. Whole blood was centrifuged at 100 g for 20 min, and the supernatant was collected and centrifuged for another 20 min. The supernatant was collected again, and 1 μM prostaglandin 1 (PGE1) was added, followed by centrifugation at 800 rpm for 20 min to collect the platelet. After a final wash with PBS containing PGE1, it was re-suspended in Tyrode's solution for preservation.

Preparation of αMM@PLTs. To prepare ultrasound-sensitive PLTs, freshly prepared αMM nanoparticles were carefully and slowly added to the PLT solutions along the test tube at a volume ratio of 1:5, mixed well and placed on a shaker to incubate for 30 min. Then, the mixed solution was centrifuged (800 rpm, 10 min) and washed three times with PBS containing 1 μM PGE1. Finally, the resulting αMM@PLTs were re-suspended in Tyrode's solution containing 1 μM PGE1 for brief storage.

The GSH and US triggered α-MT Release. For the GSH and US dependent drug release, αMM@PLTs was intervened with 3 mM GSH and US irradiation (1.0 MHz, 1.0 W cm^{-2}, 50% duty cycle, 1 min), and the released α-MT was determined by HPLC at different time intervals.

Bio-TEM Imaging. ZR-75-1 cells were co-incubated with αMM for 4 h, and lightly washed with PBS three times. Then added 2.5% glutaraldehyde electron microscope fixing solution, and fixed for 5 min at room temperature and avoided light. Finally, used a cell scraper to gently scrape the cells for TEM.

Intracellular GSH Level Assay. ZR-75-1 cells were carefully seeded into a six-well cell plate (the density is 1×10^5 cells). After 24 h of growth, the cells were incubated with PBS, αM, MM or αMM (MOF concentration 15 μg mL^{-1}) for 24 h. Then, the cells were gently washed 3 times with PBS, and the GSH level in cell was analyzed using a GSH analysis kit based on the introduction.

ROS Detection. a). ESR and DPBF. The $^1O_2$ generation ability of Zr-MOF nanoparticles was discovered by ESR qualitatively and UV–*vis* spectra quantitatively. Typically, MOF and α-MM@PLTs was exposed to US irradiation (1.0 MHz, 1.0 W cm^{-2}, 50% duty cycle, 1 min) in the existence of ROS capture agent TEMP (95 μM), and then analyzed by ESR immediately. In addition, distinct concentrations of αMM@PLTs (2, 1, and 0.5 mg mL^{-1}) were exposed to US irradiation (1.0 MHz, 1.0 W cm^{-2}, 50% duty cycle) for 1 min in the existence of DPBF (50 μl, 8 mM), and the UV–*vis* spectroscope tested the absorbance intensity at 470 nm wavelength. Furthermore, the solution was also irradiated by US under the same conditions every 1 min (0 min, 2 min, 4 min, 6 min, 8 min, 10 min) to investigate the time dependencies. b). CLSM imaging. The cellular $^1O_2$ production was detected by CLSM. The ZR-75-1 cells were first incubated with PBS, MOF, α-MT or αMM@PLTs (MOF concentration 15 μg mL^{-1}) for 4 h in 5% CO_2 at 37 °C and then replaced by DCFH-DA (10 μM). For MOF and αMM@PLTs groups, the cells were irradiated with a 1.0 MHz US at 1.0 W cm^{-2} for 1 min. After 30 min incubation, the confocal images were immediately obtained by confocal fluorescence imaging with 488 nm excitation.

Autophagy Analysis. To verify the autophagy induction effect of SDT and glutamine deprivation, ZR-75-1 cells were incubated with the autophagic dye DAPGreen (4 nM) for 30 min in a 37 °C cell incubator, then washed 3 times with PBS. The autophagosomes and autolysosomes were observed by CLSM after different treatments.

In Vitro Cytotoxicity Assay. a) CCK-8 assay. The cell killing effect of glutamine deprivation jointed with SDT was explored by the CCK-8 tests. ZR-75-1 cells were in advance seeded into cell plates and cultured for 48 h, followed by α-MM's intervention (MOF concentration 2.0, 4.0, 8.0, 16.0, 32.0, and 64.0 μg mL^{-1}). In addition, ZR-75-1 cells were also divided into five different therapeutic groups, including control, MOF, αM, αMM, αMM@PLTs. After an additional 24 h of intervention, the cell culture solutions containing nanomaterials were abandoned and replaced by CCK-8 solution diluted with PBS. After 30 min incubation, the 450-nm optical density was tested using the standard microplate reader. b) Flow cytometric analysis. The early apoptosis level of cancer cells was explored using cytoflow Annexin V-FITC/PI staining kit. Typically, after different treatments, the cells in the six-well plate were collected and re-dispersed in the buffer solution, and incubated with dyes for 10–15 min at 37 °C protected from light, followed by machine and Flow Jo software analysis. c) CLSM imaging. To intuitively observe the killing effect of nanomaterials, ZR-75-1 cells were lightly

seeded in confocal cellular dishes for CLSM imaging. After different treatments, the cancer cells were stained by calcein-AM/PI (10 μM), and incubated protected from light for 15 min. Before confocal microscopy experiments, the cells were gently washed 3 times with ice PBS.

Western Blots. For the purpose of demonstrating the expression changes of key proteins (ASNS, CHOP, S6-kP, S6-P, LC3B, GPX4, c-CAS3, c-PARP, and Lamin A) of ZR-75-1 cells after treatment, cell proteins were extracted for Western blot analysis. Briefly, after the samples were prepared, they went through the steps of sample loading and electrophoresis, transferring membrane, blocking, and antibody incubation. Finally, the gel imaging system was used to achieve visualization.

Transcriptome Analysis. Firstly, extracting total RNAs of ZR-75-1 cells from test group and control group based on the manufacturer's presentation, and then evaluating and filtering RNA by 2100 Bioanalyser and ND-2000, respectively. The qualified RNA inclusion criteria including OD260/280 = 1.8–2.2, $OD_{260/230} \geq 2.0$, RIN ≥6.5, and 28S:18S ≥ 1.0, >2 μg. Next, to establish sequencing library using the qualified RNA samples. RNA was extracted and purified, followed by reverse transcription analysis and construction of comparison libraries using Illumina HiSeq X10. To represent incremental change and statistical analysis of alterably expressed mRNAs, the changes in gene expression were defined by computing the FPKM value. The gene enrichment analysis of GO terms and KEGG signaling pathway were carried out by utilizing GO-Term Finder and DAVID, respectively.

In Vivo Bio-compatibility Assay. To evaluate the bio-compatibility of MOF and αMM@PLTs *in vivo*, 20 health experimental mice (BALB/c, 6-week-old) were at random divided into four groups (n = 5), including control, MOF, αM, and αMM@PLTs, and then intravenously administrated with 100 μl different nanomaterials (MOF concentration 5 mg kg^{-1}). Mice in the control group were given PBS. Fourteen days after injection, the blood samples and the organs of heart, liver, spleen, lung and kidney were collected for biosafety evaluation.

In Vivo Antitumor Therapy. To investigate the synergistic therapeutic effect of SDT and glutamine deprivation, 20 female BALB/c nude mice of 6 weeks old bearing ZR-75-1 tumors were divided into four groups (n = 5 in each group), including (I) control, (II) SDT, (III) α-MT, and (IV) synergistic therapy. Three intermittent administration (day 1, 3, 5) of tail-vein injection (MOF concentration 5 mg kg^{-1}, 100 μl) and US irradiation (1.0 MHz, 2.5 W cm^{-2}, 50% duty cycle, 5 min) were conducted when tumors grew to about 70 mm^3. After injection for 6 h, the tumors were exposed to low intensity focus US irradiation in groups II and IV. The tumor sizes and body weights were recorded every other day for 2 weeks after treatments, and the survival times of mice were also recorded. Tumor border dimensions were measured by caliper measurements and tumor volumes were calculated using the referenced formulas: $V = (\text{width}\ [2] \times \text{length})/2$. Tumor inhibition rates were calculated by comparing tumor weights: $\delta = (1 - W/W_0) \times 100\%$ (W_0: tumor weight of control group). The linear addition of the effects on tumor volume and tumor weight were calculated following the equation $Xc - [(Xc - Xs) + (Xc - X\alpha)]$ (X: the average value of volumes and weights). After the treatment, the tumor was dissected, sliced, and stained by H&E, Ki67, TUNEL, and GPX4 for histopathological mechanism analysis.

Statistical Analysis. Statistical comparisons were performed by SPSS 20 statistical software (version 20.0) using student's *t*-test with a setting significance of $^*P < 0.05$ (significant), $^{**}P < 0.01$ (moderately significant), and $^{***}P < 0.001$ (highly significant), respectively. All quantitative data were expressed as mean ± standard deviation (s.d.) of at least three independent experiments.

3. Results and discussion

The engineered circulating PLTs release nanomaterials at the tumor site under US stimulation and protrude pseudopodia to transform into dendritic platelets, forming thrombi to block blood supply (Fig. 1a). The nanoparticles can be successfully loaded by the PLTs through the physical adsorption of electrostatic attraction and the intrinsic endocytosis of PLTs. The pure αMM surface was positively charged (Fig. 1b), while the αMM@PLTs showed a negative zeta potential similar to that of native PLTs, indicating the successful loading of nanomaterials on PLTs (Fig. 1b). The scanning electron microscopy (SEM) images of the sonosensitive PLTs further verified that the MOF nanomaterials were encapsulated by the circulating PLTs (Fig. 1c). The loading amount of αMM on PLT was calculated based on the Mn concentration determined by inductively coupled plasma mass spectrometry (ICP-MS) in αMM@PLTs, which can reach 85 ppm. US irradiation promoted circulating PLTs to protrude pseudopodia and turn into thrombus woven into a mesh (Fig. 1c). The MOF nanoparticles were synthesized according to a

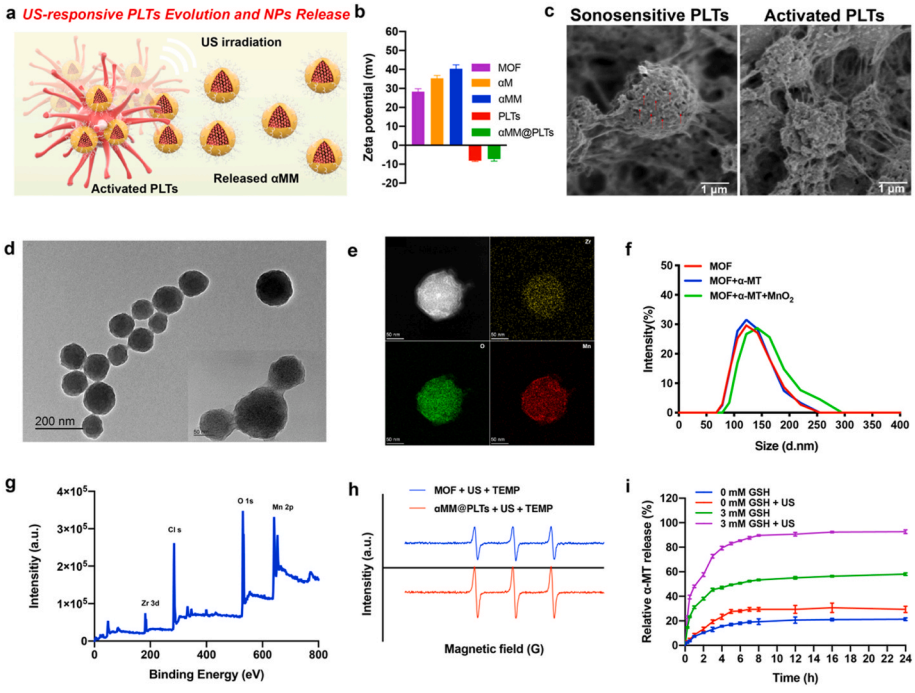

Fig. 1. Characterization of αMM@PLTs bio-nano platforms. (a) Schematic illustration showing the release of αMM nanomaterials from the sonosensitive PLTs bio-nano platform upon US stimulation. b) Zeta potential of MOF, MOF + α-MT (αM), MOF + α-MT + MnO_2 (αMM), PLTs and αMM@PLTs. Quantitative data are presented as means ± s.d. (n = 3). c) Representative SEM images of sonosensitive PLTs and activated PLTs. (d) Representative TEM images of Zr-MOF with inset showing the drug-loaded and MnO_2-coated Zr-MOF at high magnification. (e) Elemental distribution of αMM nanoparticle mapped by energy dispersive X-ray spectroscopy. (f) Average hydrodynamic size distribution of MOF, MOF + α-MT (αM), and MOF + α-MT + MnO_2 (αMM), respectively. (g) XPS spectrum revealing all the elements of αMM. (h) ESR spectra of MOF and αMM@PLTs with US irradiation (1.0 MHz, 1.0 W cm^{-2}, 50% duty cycle, 1 min). (i) GSH- and US irradiation-dependent release of α-MT from αMM@PLTs examined in PBS.

facile solvothermal method [20]. The results of transmission electron microscopy (TEM) and dynamic light scattering (DLS) indicated that the MOF nanoparticles had a roughly spherical morphology with a size distribution of approximately 124.5 nm and zeta potential of 28.7 ± 1.4 eV in charged surface (Fig. 1b, d, and f). The powder X-ray diffraction (XRD) pattern revealed that the obtained MOF accorded PCN-224 structure [20] (Fig. S1). In order to obtain α-MT-loaded MOF (αM), the prepared MOF nanoparticles were mixed with α-MT in *N, N*-dimethylformamide (DMF) and stirred for 12 h. Subsequently, a MnO_2 unlocked layer was deposited on the surface of MOF nanoparticles by reducing $KMnO_4$ with the aid of polyallylamine hydrochloride (PAH), resulting in the generation of MnO_2-coated MOF. After being encapsulated with α-MT and subsequently deposited with MnO_2 shell, the average diameter of αMM MOF nanoparticles increased to 126.1 and 146.5 nm, respectively, with the surface zeta potential maintaining positive (36.1 ± 1.7 and 40.8 ± 1.8 eV, respectively) (Fig. 1b, f). The size of drug-loaded αMM nanoparticles was experimentally stable and did not significantly change during the 7-day incubation with phosphate buffered saline (PBS) at pH 7.4 (Fig. S2). Elemental distribution based on energy dispersive X-ray spectroscopy (EDS) elemental mapping images exhibited that the Mn component was mainly deposited in the peripheral shell and Zr was distributed in the core region, implying the efficacious coating of MnO_2 shell (Fig. 1e). In addition, high intensity signals at characteristic peaks of Mn and Zr demonstrated by X-ray photoelectron spectroscopy (XPS) spectrums further provided credible evidences for the successful construction of Mn-coated Zr-MOF nanoplatform (Fig. 1g and Fig. S3). Based on the EDS spectrum of αMM and analysis data, the weight percentage (Wt%) of manganese element is about 3.73%. ICP-MS was performed to determine the manganese ion concentration in different pHs (5.5 and 7.4) and GSH concentrations (0 and 3 mM). More than 66% of Mn^{2+} is released from αMM in 3 mM GSH solution of pH 5.4 after 12 h incubation, but the proportion is only 14% in pH 7.4 solution (Fig. S4). In order to confirm whether α-MT was successfully loaded by MOF, the ultraviolet–visible (UV–*vis*) spectroscopy analysis of MOF, α-MT and αM was performed. The UV–*vis* results exhibited similar characteristic absorption peak in both α-MT and αM at about 287 nm, indicating the effective loading of α-MT in the MOF core (Fig. S5). Additionally, the increased surface Zeta potential from MOF to αM also revealed the satisfactory encapsulation (Fig. 1b). As the concentration of α-MT increased from 0.2 mg mL^{-1} to 1.6 mg mL^{-1}, the UV–*vis* absorption intensity of αM nanoparticles progressively raised and displayed an agreeable linear relationship between tested absorbance units and drug concentrations (Figs. S6 and S7). The optimized encapsulation efficiency of α-MT in αM nanoparticles was 78.3 ± 1.5% at the concentration of 0.8 mg ml^{-1} (Fig. S8).

To verify the ROS generating ability of the integrated nanoplatform under US exposure qualitatively and quantitatively, 2,2,6,6-tetramethylpiperidine (TEMP) and 1,3-diphenyliso-benzofuran (DPBF) were applied to identify the $^1O_2$ production with electron spin resonance (ESR) and UV–*vis* measurement, respectively [21]. As the results showed, representative $^1O_2$-induced signals were obviously inspected in MOF and αMM nanocomplexes, illustrating the quick generation of $^1O_2$ during the process of US irradiation (Fig. 1h). The UV–*vis* spectrum demonstrated that the absorbance intensity of DPBF at about 468 nm slowly increased with the elevation concentration, and progressively decreased with the extension of time, indicating a concentration- and time-dependent ROS generation of nanoparticles (Fig. S9). The MnO_2 wrapped in the outer layer of MOF not only plays a role in preventing drug leakage, but also achieves targeted drug delivery in response to excessive GSH in TME. When αMM nanoparticles were incubated in a certain concentration of GSH solution (4×10^{-3} M), the solution color varied significantly from dark yellow to light yellow within 5 min (Fig. S10), suggesting the effective degradation of MnO_2. The GSH-triggered cumulative release experiment demonstrated that the release rate only reached about 20% of encapsulated α-MT in the absence of GSH, and after adding 3×10^{-3} M GSH, it reached about 50% within 24 h. Especially, US irradiation further stimulated drug release through resonance effects with an increased release rate of approximately 90% (Fig. 1i). The acidic tumor microenvironment also promoted the drug release due to the degradation reaction of hydrogen ions to the MnO_2 shell (Fig. S11).

To demonstrate the MnO_2-induced GSH-scavenging activity and α-MT-inhibited GSH synthesis of αMM@PLTs, an intracellular GSH assay was performed on ZR-75-1 breast cancer cells by UV–*vis* spectroscopy analysis. After being treated with simple MOF core, the GSH levels in ZR-75-1 cells did not occur with significant change. Comparatively, the incubation with α-MT-loaded MOF (αM), MnO_2-coated MOF (MM), and αMM@PLTs for 5 h resulted in a remarkable intracellular GSH concentration reduction of at least 40%, and αMM@PLTs exhibited the strongest GSH eliminating ability, implying the synergistic inhibitory effects of endogenous and exogenous interventions (Fig. 2a). To determinate whether blockade of SLC6A14 transporter brings about amino acid starvation in breast cancer cells, the SLC6A14-positive breast cancer cell line ZR-75-1 were treated with αMM@PLTs for 24 h and 48 h under US irradiation, and then the expressions of asparagine synthetase (ASNS) and C/EBP-homologous protein (CHOP) were tracked as strong evidence of amino acid starvation, which were known to be increased during amino acid deficiency [22]. As illustrated in Fig. 2b and Fig. S12a, the expressions of ASNS and CHOP were significantly upregulated in αMM treatment groups. As the time was extended to 48 h, the protein expression level increased more obviously, as a consequence of SLC6A14 transporter blockaded that stimulates endogenous negative feedback regulation mechanisms, indicating the successful induction of amino acid starvation. The evolutionarily conserved mTORC1 is a foremost regulator of cell growth via activating protein translation and inhibiting macroautophagy in response to external stimuli, such as amino acid abundance, growth factor signaling, or others [23]. Substantial evidence sustains the critical role of amino acids in regulating the activation of mTORC1 dependent signaling, especially the glutamine metabolism [24]. Blocking the SLC6A14 transporter to inhibit glutamine uptake enables the inactivation of mTORC1 signaling pathway, thus inhibiting tumor cell growth and activating autophagy. The evidence of mTOR inhibition on ZR-75-1 cells when treated with α-MT was proved by a down-regulated expression in the phosphorylation of mTOR's downstream targets S6 and S6 kinase (Fig. 2b, Fig. S12a).

The intracellular ROS generation level of SDT using MOF nanosonosensitisers was subsequently confirmed by raising confocal laser scanning microscopy (CLSM) fluorescence intensity of $^1O_2$-sensitive dye (2′,7′- dichlorofluorescein diacetate, DCFH-DA) stained breast cancer cells [25,26] (Fig. 2c). A great amount of ROS generated by SDT also triggered the occurrence of cellular autophagy [27]. As mentioned above, the blockade of glutamine-dependent activation of mTORC1 also upregulated cellular protective autophagy as a part of the survival mechanism by inhibiting mTORC1 translocation to lysosomes [28]. The detailed therapeutic mechanism of αMM under US irradiation was illustrated in Fig. 2d. Treatment of ZR-75-1 cells with α-MT and SDT induced autophagy as evident from the visible presence of autophagosomes in DAPGreen stained confocal fluorescence images analysis [29] (Fig. S13), the significantly increased LC3-II protein expression in immunoblot analysis [30] (Fig. 2e, Fig. S12b), and the apparent autophagic flux in bio-TEM evaluation [31] (Fig. 2h). The cellular DNA damage effect of αMM@PLT on enhancing tumor suppression response was evaluated by using a specific marker-γ-H2AX staining. As expected, the significant γ-H2AX fluorescence was observed in the nuclei site of breast cancer cells when incubated with αMM@PLT and irradiated with US, indicating an increased DNA damage of the combined treatment (Fig. 2f). The bio-TEM images showed that the as-prepared αMM nanoparticles were efficiently endocytosed into cancer cells after 4 h incubation (Fig. 2g). Additionally, unlocking of endogenous consumption and blocking of exogenous synthesis of GSH by αMM nanoplatform were conducive to trigger ferroptosis, demonstrated by the changed expression of ferroptosis marker protein GPX4 in WB analysis [32]

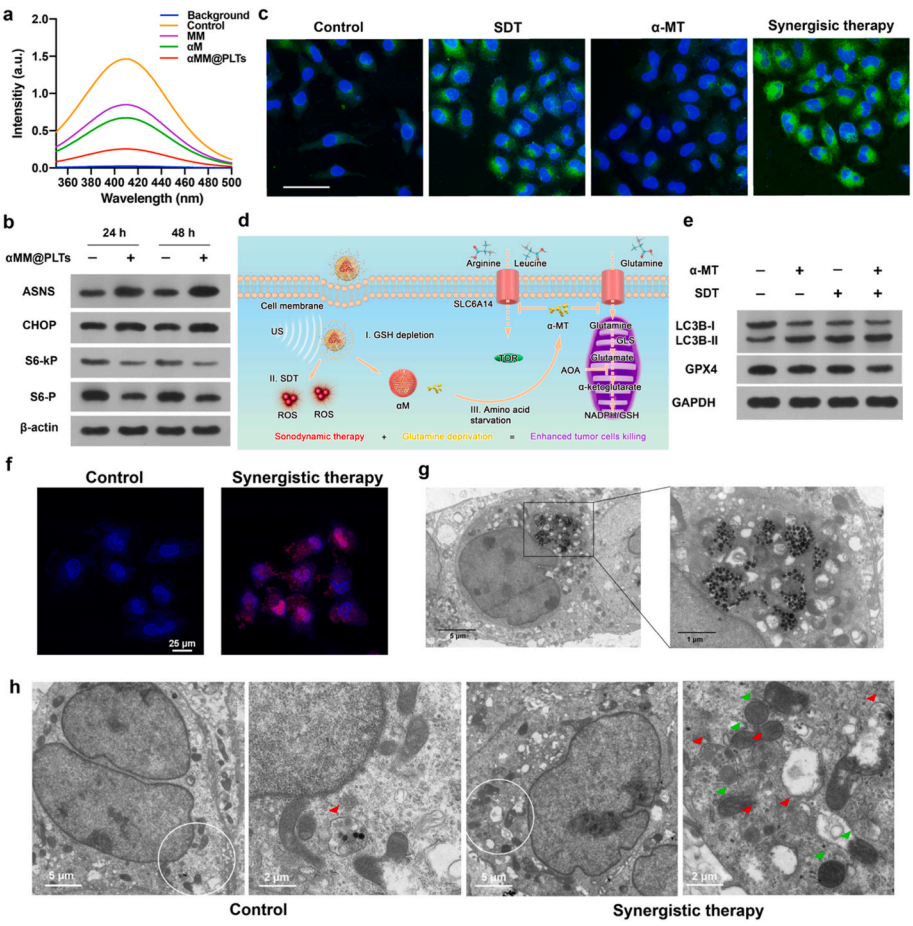

Fig. 2. ***In vitro*** **exploration of αMM@PLTs bio-nano platform's therapeutic mechanism.** (a) UV–*vis* absorption spectrum evaluation of intracellular GSH consumption capacity of different nanoplatforms. (b) Western blot analysis on the protein expression of ASNS, CHOP, S6-kP, and S6-P after different treatments. β-Actin was used as a loading control. (c) CLSM analysis of breast cancer cells stained by DCFH-DA for intracellular ROS after different treatments. Scale bars, 40 μm. (d) Schematic diagram of glutamine deprivation for synergistic sonodynamic cancer therapy. (e) Western blot analysis on the expressions of autophagy indicator proteins LC3B and key ferroptosis makers GPX4 after different treatments. GAPDH was used as a loading control. (f) Representative DNA damage marker γ-H2AX assays of breast cancer cells after synergistic treatment. (g) TEM assessment of phagocytic behavior of nanomaterials by cancer cells. (h) Bio-TEM images of ZR-75-1 cells treated with PBS (Control), and αMM@PLTs + US (Synergistic therapy). Red arrows indicate autophagosome and green arrows indicate the smaller, ruptured mitochondria.

(Fig. 2e, Fig. S12b) and the unique morphological characteristics of ferroptosis in bio-TEM evaluation, such as mitochondrial atrophy, increased mitochondrial membrane density and disappearance of mitochondrial ridges [33] (Fig. 2h). Especially, the autophagic degradation process of ferritin could augment susceptibility to ferroptosis by effectively raising the content of unstable iron pools in cells [34], thereby expanding the killing effect of SDT due to inducing "mixed" types of cell death (apoptosis/ferroptosis) [35]. All these results suggested that αMM nanoparticles could efficaciously induce amino acid starvation, inhibit mTOR, activate ferroptosis, and ultimately achieve synergistically amplified sonodynamic tumor treatment.

To investigate the anti-proliferation effects of glutamine deprivation in breast cancer, we quantitatively measured the viabilities of ZR-75-1 cells cultured for 24 h and 48 h in media with varying concentrations of αMM@PLTs by a typical cell-counting kit-8 (CCK-8) assay (Fig. 3a). Substantial proliferation inhibition effect was observed when the αMM concentration was elevated to 8.0 μg mL^{-1} for 24 h amino acid blocking. With the extension of glutamine blocking time to 48 h, the cytotoxic impacts became much stronger. We then sought to explore the elevated synergistic anti-tumor effect induced by glutamine deprivation and SDT (Fig. 3b). It has been found that the SDT-induced oxidative stress damage could be adequately heightened in GSH-blocked manners via MnO_2-induced GSH scavenging and α-MT-inhibited GSH synthesis. Since SLC6A14 is a broad-spectrum cell transporter, apart from glutamine deprivation, it is speculated that other amino acid blockade may also produce heightened tumor cell-killing effect. In addition, due to the existence of cellular protective autophagy induced by SDT and glutamine deprivation, we thus attempted to further treat tumor cells with an autophagy inhibitor 3-methyladenine (3-MA) [36]. As expected, the co-treatment of ZR-75-1 cancer cells with 3-MA did not augment cell death, verifying the above hypothesis of the positive role of autophagy in ferroptosis modulation [37].

The underlying molecular mechanism of cell apoptotic death was further explored by Western blot analysis (Fig. 3c and d). Cleaved caspase 3 (c-CAS3), a typical pro-apoptotic enzyme, was exceedingly upregulated in ZR-75-1 cell line after cooperative treatment, verifying the apoptosis pathway after synergistic sonodynamic tumor therapy [38]. As a specific substrate of caspase widely related with cellular response to DNA damage and metabolism, cleaved poly ADP ribose polymerase (c-PARP) was remarkably activated in the combinational therapy group, evidencing that the synergy between SDT and glutamine deprivation could result in unique DNA-strand break and abnormal epigenetic adjustment of chromatin structure, thus directing cancer cells to enter the apoptosis pathway [39]. Lamin proteins are structural components of the nuclear membrane that play a central role in keeping important cellular functions such as control of the cell cycle, DNA replication, etc. [40,41]. During the process of apoptosis, lamin A can be expressly cleaved by Caspase-6 and act as a marker of nuclear dysregulation and cell death [42]. As a specific substrate for activated caspase-6, the cleavage of lamin A in the synergistic treatment group also indicated the apoptotic cell death. The morphological and functional changes of PLTs under US stimulation play a key role in tumor therapy, as activated PLTs coagulate with fibrin and block the tumor's blood supply (Fig. 3e). Calcein-AM and propidium iodide (PI) staining for live and dead cells by CLSM demonstrated that the synergistic therapy group achieved the best inhibitory effect of tumor cells compared with two other monotherapy strategies [43] (Fig. 3f). The flow cytometry analysis demonstrated that the overall apoptotic rate of ZR-75-1 cells after intervention with αMM@PLTs under US irradiation was as high as 60.4%, and the αM + US group and MOF + US group were

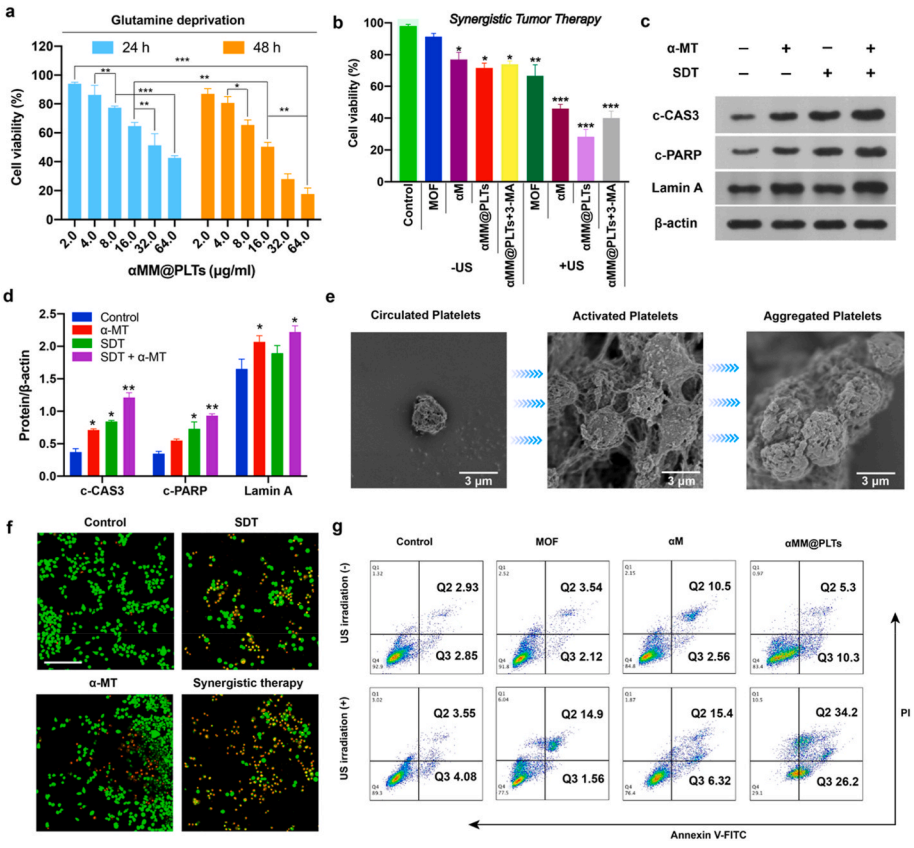

Fig. 3. Cytotoxicity of enhanced tumor cell killing of αMM@PLTs *in vitro*. (a) Cell viability assays of ZR-75-1 cells treated with αMM@PLTs for 24 h or 48 h at different concentrations of MOF. Values are presented as means ± s.d. (n = 3). $^{*}P < 0.05$, $^{**}P < 0.01$, $^{***}P < 0.001$. (b) Cell viability assays of ZR-75-1 cells treated with PBS, MOF, αM, αMM@PLTs, and αMM@PLTs + 3-MA under US irradiation (1.0 MHz, 1.0 W cm^{-2}, 50% duty cycle, 1 min). Values are presented as means ± s.d. (n = 3). $^{*}P < 0.05$, $^{**}P < 0.01$, $^{***}P < 0.001$. (c, d) Western blot and quantitative analysis on the protein expression of c-CAS3, c-PARP, and Lamin A after different treatments. β-Actin was used as a loading control. Quantitative data are presented as means ± s.d. (n = 3). $^{*}P < 0.05$, $^{**}P < 0.01$. (e) Morphological evolution from circulated PLTs to activated and aggregated PLTs in vitro. (f) CLSM evaluation of tumor cells for live/dead cells identification treated with PBS (Control), SDT, α-MT, and SDT + α-MT (Synergistic therapy). Scale bars, 60 μm. (g) Flow cytometric analysis on the apoptosis levels of ZR-75-1 cells treated with PBS, MOF, αM, and αMM@PLTs under US irradiation (1.0 MHz, 1.0 W cm^{-2}, 50% duty cycle, 1 min).

respectively 21.72% and 16.46%, which were all significantly higher than no US irradiation groups (Fig. 3g). Therefore, it is clear that oxidative stress reaction generated by MOF nanoparticles under US irradiation could be effectively heightened by MnO_2-induced GSH scavenging and α-MT-caused glutamine deprivation.

To further elaborate the potential synergistic anti-tumor mechanisms, transcriptomics analysis was carried out to quest the gene variances of ZR-75-1 breast cancer cells [44]. The heat map data and principal component analysis (PCA) illustrated significant changes of gene expression between the control group and test group (Fig. 4a and b). The Venn diagram evidenced that the control and test groups co-expressed 10 740 genes, while the test group exclusively expressed 235 genes (Fig. 4c). Under the defined screening criteria, 173 distinctively expressed mRNAs were found to be associated with the synergistic therapeutic process of glutamine deprivation-enhanced SDT, of which 105 were up-regulated and 68 were down-regulated (Fig. 4d). Kyoto

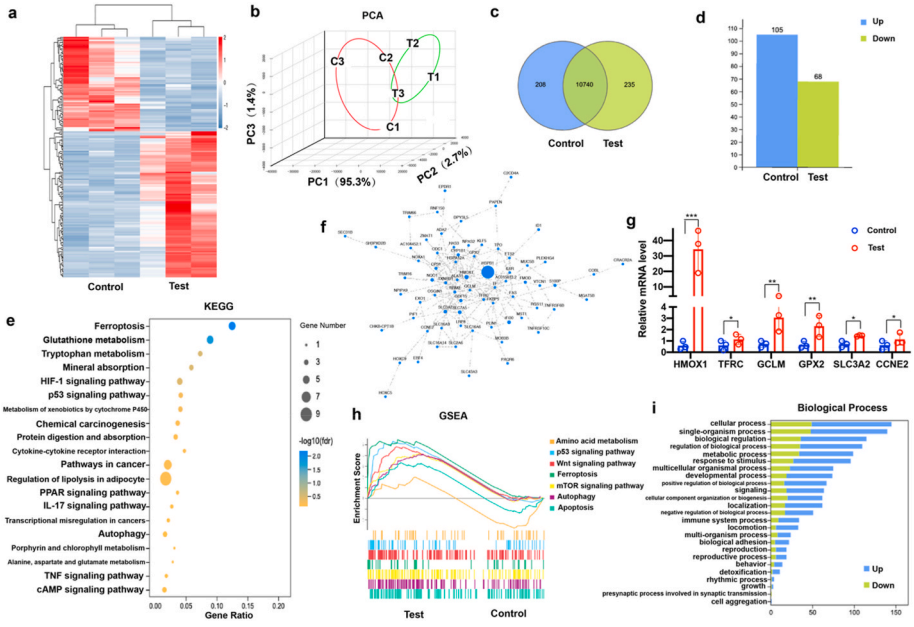

Fig. 4. Transcriptome sequencing analysis of mRNA expressions after synergistic therapy. (a, b) Heat map diagram and principal component analysis based on differentially expressed genes from the control and test groups. (c) Venn diagram of the transcriptomic profiles between control group and synergistic therapy group. (d) Overall statistics of differential genes. (e) Kyoto Encyclopedia of Genes and Genomes (KEGG) pathway analysis of differential genes. (f) Protein-protein interaction network assay. (g) PCR analysis of genes involved in significant signaling pathways. (h) Gene set enrichment analysis (GSEA) for certain signaling pathways related synergistic therapy. (i) Biological process of up-regulated and down-regulated genes.

Encyclopedia of Genes and Genomes (KEGG) pathway enrichment analysis demonstrated that ferroptosis, autophagy, and amino acid metabolism were obviously connected with the anti-tumor mechanisms of αMM@PLTs under US irradiation, which were highly consistent with previous forecasts (Fig. 4e). Blocking the uptake of amino acids by α-MT inhibited the synthesis of GSH, coupled with the consumption of intracellular GSH by MnO_2, and synergistically promoted the occurrence of ferroptosis [45]. In addition, the large accumulation of intracellular ROS caused by SDT could promote lipid peroxidation reaction, thereby promoting cell ferroptosis [46]. Cell-selective autophagy induced by SDT stimulation and amino acids starvation effectively regulated the sensitivity of ferroptosis through degrading iron storage protein ferritin and increasing the levels of intracellular labile iron pool (LIP) [34]. Targeting ferroptosis enables the improvement of tumor sensitivity to pro-apoptotic therapy [47]. The genes associated with the above signaling pathways that significantly changed after synergistic treatment were utilized in the network analysis of protein-protein interactions (Fig. 4f). Validation analysis of Polymerase Chain Reaction (PCR) revealed that, the expression of mRNA related to the above-mentioned signal pathway, including HMOX1, TFRC, GCLM, GPX2, SLC3A2, and CCNE2, were significantly upregulated after the synergistic treatment (Fig. 4g and Table S1). Gene set enrichment analysis (GSEA) also verified these results, showing that changed expressed mRNAs were significantly enriched in signaling pathways of amino acid metabolism, mTOR signaling pathway, autophagy, ferroptosis, and apoptosis (Fig. 4h). Gene Ontology (GO) analysis was also conducted on the mRNAs with up-regulated and down-regulated expression level through the field of biological process, molecular

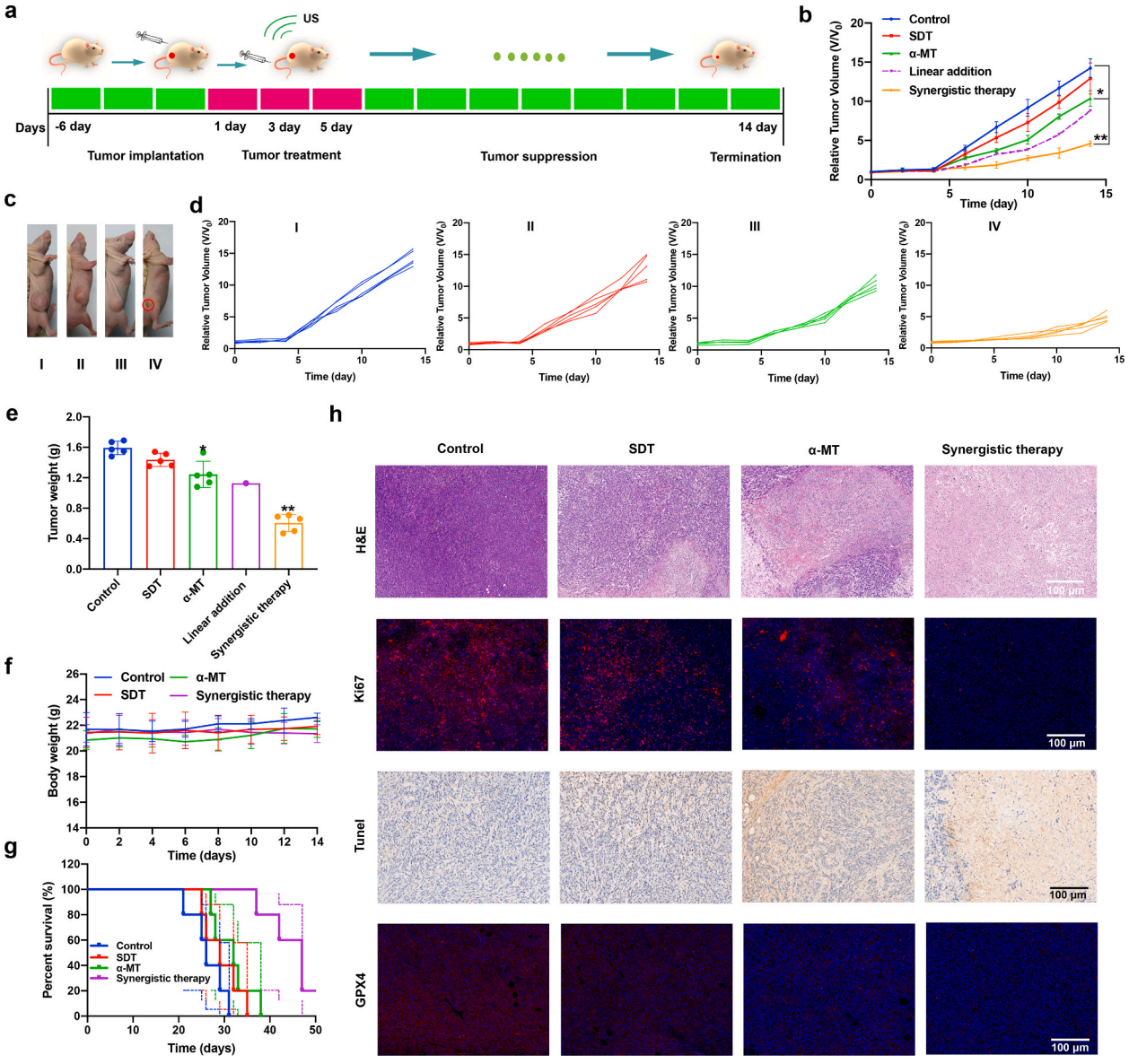

Fig. 5. ***In vivo*** **anticancer activity of SDT and glutamine deprivation**. (a) *In vivo* therapeutic schedule of αMM@PLTs under US irradiation (1.0 MHz, 2.5 W cm^{-2}, 50% duty cycle, 5 min) (n = 5). (b) Relative tumor volume growth curves during the 14-day therapeutic period. Values are presented as means ± s.d. (n = 5). $^{*}P < 0.05$, $^{**}P < 0.01$. (c) Typical comparative photographs of tumor size of mice in each therapeutic group. This red circle-marked tumor represents a shrinking and thrombosed tumor. (d) Individual tumor growth curves of mice after different treatments of I (Control), II (SDT), III (α-MT), and IV (Synergistic therapy). (e) Final weights of the excised tumors on the 14th day. Values are presented as means ± s.d. (n = 5). $^{*}P < 0.05$, $^{**}P < 0.01$. (f) Variations of average body weight of tumor-bearing mice during 14-day treatments (n = 5). (g) Survival curves of tumor-bearing mice with different treatments during 50 days of monitoring (n = 5). The dotted line represents the 95% confidence interval (CI). (h) Representative immunohistochemical (H&E and TUNEL) and immunofluorescence (Ki67 and GPX4) staining images of excised tumors from different groups after 14 days' treatments.

function and cellular component (Fig. 4i and Fig. S14). The induction of multiple cell death modes (autophagy, ferroptosis, and apoptosis) can maximize the synergistic effect of tumor suppression, thus providing strategies for efficient tumor therapy.

Efficacious research into the synergistic therapy of SDT combined with glutamine deprivation of ZR-75-1 cell line in vitro spurred the testing of αMM@PLTs bio-nano platform under US irradiation as therapeutics *in vivo*. Before conducting animal treatments, we firstly performed *in vivo* bio-distribution assessment of nanomaterials *via* an *in vivo* fluorescence imaging system (IVFIS). The results showed that αMM@PLTs bio-nano platforms could effectively accumulate at the tumor site through platelets' natural active-targeting characteristics to the TME, which ensured the reliability of anti-tumor treatment *in vivo* [48] (Fig. S15). BALB/c mice bearing ZR-75-1 tumors (≈70 mm^3) were divided into four groups randomly and treated with: 1) PBS (Control); 2) MOF + US (SDT); 3) MOF + α-MT (α-MT); 4) αMM@PLTs + US (Synergistic therapy) for two weeks. The intervention was repeated every two days for a total of 3 times with US irradiation (1.0 MHz, 2.5 W cm^{-2}, 50% duty cycle, 5 min) applied 6 h post-injection (Fig. 5a). The synergistic therapy group treated by αMM@PLTs-based SDT achieved considerable efficacy with the tumor volume of mice only slightly increased at the end of experiment (Fig. 5b–d), revealing remarkably advantageous inhibitory effect than the other two groups. Interestingly, SDT group exhibited potent tumor suppressor effect in the early stages of exploration, while after a few days the tumor restored fast growing, indicating the consolidation with glutamine deprivation was indispensable to maintain the long-term therapeutic effect of SDT. However, the α-MT group did not demonstrate distinct tumor-suppressing effect without US irradiation, probably representing that the amino acid blocking drug was much more valid as a supplement therapeutic for SDT tumor cell killing, than as an anti-tumor agent used alone in our model. It should be particularly emphasized that glutamine deprivation cooperated with SDT complied super-additive therapeutic efficacy since the tumor suppression effect of PLTs-achieved synergistic therapy is much more superior than the linear addition of monotherapies. This may be due to the inherent GSH synthesis function of cells that reduces the oxidative stress damage ability of SDT and improves the ROS resistance of cancer cells, while pharmacological glutamine depletion is effective in suppressing generation of exogenous GSH, finally heightening the sensitivity of SDT and maximizing the synergistic inhibition effect of tumor growth. In addition, US-stimulated cascading thrombosis also contributes to the inhibition of the growth and vitality of tumor through blocking blood supply. Referring to the changes in tumor weight in these groups, tumor inhibition rates were calculated to be 9.8%, 21.9%, and 57.9% for SDT, α-MT, and synergistic therapy, respectively (Fig. 5e). All mice did not occur observable changes in body weight during the entire investigation period (Fig. 5f). In accordance with the Kaplan-Meier survival curves [49], the lifespan of mice in combinational therapy group was notably extended compared with the other three groups of mice (Fig. 5g), further evidencing the exceptional therapeutic effect of the ingenious combination of SDT and glutamine deprivation based on natural PLTs bioplatform.

After the end of intervention procedures, the obtained tumors were sectioned and histologically inspected (Fig. 5h). The results of hematoxylin and eosin (H&E) staining for necrosis analysis and terminal deoxynucleotidyl transferase dUTP nickend labeling (TUNEL) staining for apoptosis analysis showed that αMM@PLTs with US irradiation group induced the most severe degree of cellular damage among all nanoplatforms. The tumor proliferation marker-Ki67 protein declined more remarkably in PLTs-based synergistic intervention group than monotherapy SDT and α-MT groups, indicating the heightened tumor killing ability [50]. Ferroptosis representative protein GPX4 was then examined to confirm the occurrence of "mixed" cell death caused by SDT and GSH deprivation [32]. For the tumors treated with monotherapy (α-MT or SDT), a markedly higher level GPX4 expression than control group was observed, and the synergistic therapeutic group yielded the highest level of ferroptotic cell death change. This verified that both SDT and amino acid starvation treatment could trigger ferroptosis, and also laid the foundation for the implementation of regulated cell death strategy to achieve better tumor treatment effect [51]. Taken collectively, the results presented here revealed that PLTs bioplatform-delivered αMM nanoparticles synergistically promoted the oxidative stress response of SDT, and the glutamine deprivation-based association was probably the major factor leading to the augmented antitumor ability of αMM. The blockade of tumor blood supply through thrombus formation also conduced to this augmentation.

To ascertain the biocompatibility of MOF nanoparticles, we dissected the major organs of nanoparticle-treated mice at the end of experiment, and conducted the corresponding histological examination, which signaled no palpable damage (Fig. S16). In addition to the histological evaluations of major organs, blood samples were also collected for serum biochemical analysis before mice were sacrificed. The results of blood indexes for routine blood, liver and kidney function also exhibit no overt change in each group of mice (Fig. S17). All these results indicated the high biocompatibility and low toxicity of αMM@PLTs bio-nano platform throughout the tumor therapeutic period.

4. Conclusions

In summary, we have developed the distinct sonosensitive PLT pharmacytes to mediate cascaded delivery of the engineered porphyrinic MOF nanostructures for achieving synergistically augmented sonodynamic anticancer therapy by stimuli-responsive glutamine deprivation and blood blockade. The nanoengineered PLT pharmacytes simultaneously acted as SDT agents and drug delivery vehicles, with the ability of active tumor targeting and ultrasonic spatiotemporally controlled release of nanomaterials. The MOF released precisely at the tumor site can not only exogenously consume the excess GSH inside cells through the surface-deposited MnO_2 shell, but also specifically block amino acid transporter SLC6A14 through the α-MT drug contained inside, therefore inducing glutamine deprivation and achieving desirable collaborative effects on SDT. Furthermore, US radiation enabled the morphological and functional changes of PLTs from circulating transport PLTs to dendritic coagulation PLTs, which promote thrombosis and block tumor blood supply, further increasing the likelihood of complete tumor eradication. It was demonstrated that the drug-loaded living cell bio-nano platform induced optimal sonodynamic anti-cancer efficiency by adopting double additive intervention of glutamine deprivation and cascading thrombosis, and performed negligible side effects and favorable biocompatibility, thereby offering a bioinspired design strategy to improve SDT efficiency, and rending an innovative paradigm for cooperatively ablating refractory tumor.

Declaration of competing interest

The authors declare no known competing financial interest.

Statement

All animal experiments were performed in accordance with relevant animal care guidelines and were approved by the Ethics Committee of Shanghai University.

Declaration of competing interest

The authors declare no competing financial interest.

CRediT authorship contribution statement

Liqiang Zhou: conceived this study and designed the experiments, performed material synthesis, characterization and analyzed the data, conducted the cellular studies and analyzed the data, carried out the in

vivo studies and analyzed the data, analyzed the results and wrote the manuscript. **Wei Feng:** performed material synthesis, characterization and analyzed the data. **Yuhang Mao:** performed material synthesis, characterization and analyzed the data, carried out the in vivo studies and analyzed the data. **Yu Chen:** analyzed the results and wrote the manuscript, conceived this study and designed the experiments. **Xuanjun Zhang:** conceived this study and designed the experiments, analyzed the results and wrote the manuscript. All authors revised this manuscript.

Acknowledgment

This work was supported by the Science and Technology Development Fund, Macau SAR (Grant No. 0114/2019/A2, 0085/2020/A2); the Research Grant of University of Macau (Grant No. MYRG2020-00130-FHS). We also thank the Internal Grant from MOE Frontiers Science Center for Precision Oncology, University of Macau and the core facilities in the Faculty of Health Sciences, especially the drug development core, bioimaging and stem cell core, and animal research core for their excellent services.

Appendix A. Supplementary data

Supplementary data to this article can be found online at https://doi.org/10.1016/j.bioactmat.2022.11.020.

References

[1] M. Oginuma, Y. Harima, O.A. Tarazona, M. Diaz-Cuadros, A. Michaut, T. Ishitani, F. Xiong, O. Pourquie, Intracellular pH controls WNT downstream of glycolysis in amniote embryos, Nature 584 (7819) (2020) 98–101.
[2] D.N. Edwards, V.M. Ngwa, A.L. Raybuck, S. Wang, Y. Hwang, L.C. Kim, S.H. Cho, Y. Paik, Q. Wang, S. Zhang, H.C. Manning, J.C. Rathmell, R.S. Cook, M.R. Boothby, J. Chen, Selective glutamine metabolism inhibition in tumor cells improves antitumor T lymphocyte activity in triple-negative breast cancer, J. Clin. Invest. 131 (4) (2021).
[3] B.J. Altman, Z.E. Stine, C.V. Dang, From Krebs to clinic: glutamine metabolism to cancer therapy, Nat. Rev. Cancer 16 (10) (2016) 619–634.
[4] A. Nilsson, J.R. Haanstra, M. Engqvist, A. Gerding, B.M. Bakker, U. Klingmuller, B. Teusink, J. Nielsen, Quantitative analysis of amino acid metabolism in liver cancer links glutamate excretion to nucleotide synthesis, Proc. Natl. Acad. Sci. U. S. A. 117 (19) (2020) 10294–10304.
[5] L. Jiang, A.A. Shestov, P. Swain, C. Yang, S.J. Parker, Q.A. Wang, L.S. Terada, N. D. Adams, M.T. McCabe, B. Pietrak, S. Schmidt, C.M. Metallo, B.P. Dranka, B. Schwartz, R.J. DeBerardinis, Reductive carboxylation supports redox homeostasis during anchorage-independent growth, Nature 532 (7598) (2016) 255–258.
[6] D.E. Lee, J.E. Yoo, J. Kim, S. Kim, S. Kim, H. Lee, H. Cheong, NEDD4L downregulates autophagy and cell growth by modulating ULK1 and a glutamine transporter, Cell Death Dis. 11 (1) (2020) 38.
[7] A.S. Krall, H.R. Christofk, Rethinking glutamine addiction, Nat. Cell Biol. 17 (12) (2015) 1515–1517.
[8] S. Karunakaran, N.S. Umapathy, M. Thangaraju, T. Hatanaka, S. Itagaki, D. H. Munn, P.D. Prasad, V. Ganapathy, Interaction of tryptophan derivatives with SLC6A14 (ATB0,+) reveals the potential of the transporter as a drug target for cancer chemotherapy, Biochem. J. 414 (3) (2008) 343–355.
[9] N. Gupta, S. Miyauchi, R.G. Martindale, A.V. Herdman, R. Podolsky, K. Miyake, S. Mager, P.D. Prasad, M.E. Ganapathy, V. Ganapathy, Upregulation of the amino acid transporter ATB0,+ (SLC6A14) in colorectal cancer and metastasis in humans, Biochim. Biophys. Acta 1741 (1–2) (2005) 215–223.
[10] N. Gupta, P.D. Prasad, S. Ghamande, P. Moore-Martin, A.V. Herdman, R. G. Martindale, R. Podolsky, S. Mager, M.E. Ganapathy, V. Ganapathy, Up-regulation of the amino acid transporter ATB(0,+) (SLC6A14) in carcinoma of the cervix, Gynecol. Oncol. 100 (1) (2006) 8–13.
[11] Q. Zhao, Z. Gong, Z. Li, J. Wang, J. Zhang, Z. Zhao, P. Zhang, S. Zheng, R.J. Miron, Q. Yuan, Y. Zhang, Target reprogramming lysosomes of $CD8^+$ T cells by a mineralized metal-organic framework for cancer immunotherapy, Adv. Mater. 33 (17) (2021), e2100616.
[12] R.S. Karunakaran S, V. Coothankandaswamy, et al., SLC6A14 (ATB0, +) protein, a highly concentrative and broad specific amino acid transporter, is a novel and effective drug target for treatment of estrogen receptor-positive breast cancer, J. Biol. Chem. 286 (36) (2011) 31830–31838.
[13] C. Zhang, L. Xin, J. Li, J. Cao, Y. Sun, X. Wang, J. Luo, Y. Zeng, Q. Li, Y. Zhang, T. Zhang, P. Huang, Metal-organic framework (MOF)-Based ultrasound-responsive dual-sonosensitizer nanoplatform for hypoxic cancer therapy, Adv. Healthc. Mater. 11 (2) (2022), e2101946.
[14] M. Xu, L. Zhou, L. Zheng, Q. Zhou, K. Liu, Y. Mao, S. Song, Sonodynamic therapy-derived multimodal synergistic cancer therapy, Cancer Lett. 497 (2021) 229–242.
[15] L.Q. Zhou, P. Li, X.W. Cui, C.F. Dietrich, Ultrasound nanotheranostics in fighting cancer: advances and prospects, Cancer Lett. 470 (2020) 204–219.
[16] Q. Zeng, X. Ma, Y. Song, Q. Chen, Q. Jiao, L. Zhou, Targeting regulated cell death in tumor nanomedicines, Theranostics 12 (2) (2022) 817–841.
[17] S. Tang, F. Zhang, H. Gong, F. Wei, J. Zhuang, E. Karshalev, B. Esteban-Fernandez de Avila, C. Huang, Z. Zhou, Z. Li, L. Yin, H. Dong, R.H. Fang, X. Zhang, L. Zhang, J. Wang, Enzyme-powered Janus platelet cell robots for active and targeted drug delivery, Sci. Robot 5 (43) (2020).
[18] A.M. Vargason, A.C. Anselmo, S. Mitragotri, The evolution of commercial drug delivery technologies, Nat. Biomed. Eng. 5 (9) (2021) 951–967.
[19] B. Bahmani, H. Gong, B.T. Luk, K.J. Haushalter, E. DeTeresa, M. Previti, J. Zhou, W. Gao, J.D. Bui, L. Zhang, R.H. Fang, J. Zhang, Intratumoral immunotherapy using platelet-cloaked nanoparticles enhances antitumor immunity in solid tumors, Nat. Commun. 12 (1) (2021) 1999.
[20] J. Park, Q. Jiang, D. Feng, L. Mao, H.C. Zhou, Size-controlled synthesis of porphyrinic metal-organic framework and functionalization for targeted photodynamic therapy, J. Am. Chem. Soc. 138 (10) (2016) 3518–3525.
[21] O. Zgadzai, Y. Twig, H. Wolfson, R. Ahmad, P. Kuppusamy, A. Blank, Electron-spin-resonance dipstick, Anal. Chem. 90 (13) (2018) 7830–7836.
[22] M.S. Kilberg, J. Shan, N. Su, ATF4-dependent transcription mediates signaling of amino acid limitation, Trends Endocrinol. Metabol. 20 (9) (2009) 436–443.
[23] S. Wullschleger, R. Loewith, M.N. Hall, TOR signaling in growth and metabolism, Cell 124 (3) (2006) 471–484.
[24] S.G.a.T.G. Dann, The amino acid sensitive TOR pathway from yeast to mammals, FEBS Lett. 580 (2006) 2821–2829.
[25] P. Zhu, Y. Chen, J. Shi, Nanoenzyme-augmented cancer sonodynamic therapy by catalytic tumor oxygenation, ACS Nano 12 (4) (2018) 3780–3795.
[26] A. Gomes, E. Fernandes, J.L. Lima, Fluorescence probes used for detection of reactive oxygen species, J. Biochem. Biophys. Methods 65 (2–3) (2005) 45–80.
[27] L. Zhou, M. Huo, X. Qian, L. Ding, L. Yu, W. Feng, X. Cui, Y. Chen, Autophagy blockade synergistically enhances nanosonosensitizer-enabled sonodynamic cancer nanotherapeutics, J. Nanobiotechnol. 19 (1) (2021) 112.
[28] P. Nicklin, P. Bergman, B. Zhang, E. Triantafellow, H. Wang, B. Nyfeler, H. Yang, M. Hild, C. Kung, C. Wilson, V.E. Myer, J.P. MacKeigan, J.A. Porter, Y.K. Wang, L. C. Cantley, P.M. Finan, L.O. Murphy, Bidirectional transport of amino acids regulates mTOR and autophagy, Cell 136 (3) (2009) 521–534.
[29] S.H. Iwashita H, N. Nagahora, et al., Small fluorescent molecules for monitoring autophagic flux, FEBS Lett. 592 (4) (2018) 559–567.
[30] U.T. Tanida I, E. Kominami, LC3 and autophagy, Methods Mol. Biol. 445 (2008) 77–88.
[31] B.S. Glick D, K.F. Macleod, Autophagy: cellular and molecular mechanisms, J. Pathol. 221 (1) (2010) 3–12.
[32] S.R. Yang WS, M.E. Welsch, et al., Regulation of ferroptotic cancer cell death by GPX4, Cell 156 (1–2) (2014) 317–331.
[33] S.B. Hirschhorn T, The development of the concept of ferroptosis, Free Radic. Biol. Med. 133 (2019) 130–143.
[34] X.Y. Hou W, X. Song, et al., Autophagy promotes ferroptosis by degradation of ferritin, Autophagy 12 (8) (2016) 1425–1428.
[35] L. Zhou, W. Feng, L. Chen, H. Huang, S. Huang, Q. Chen, X. Zhang, Y. Chen, Targeting acidogenic metabolism by engineering self-catalytic siRNA nanocarriers/nanocatalysts for amplified tumor apoptosis/ferroptosis, Nano Today 46 (2022).
[36] T.M. Shi Y, X. Ma, et al., Delayed treatment with an autophagy inhibitor 3-MA alleviates the progression of hyperuricemic nephropathy, Cell Death Dis. 11 (6) (2020) 467.
[37] K.F. Liu J, G. Kroemer, D.J. Klionsky, R. Kang, D. Tang, Autophagy-dependent ferroptosis: machinery and regulation, Cell Chem. Biol. 27 (4) (2020) 420–435.
[38] M. Brentnall, L. Rodriguez-Menocal, R.L. De Guevara, E. Cepero, L.H. Boise, Caspase-9, caspase-3 and caspase-7 have distinct roles during intrinsic apoptosis, BMC Cell Biol. 14 (2013) 32.
[39] V.D.F. Schreiber, J.C. Ame, G. de Murcia, Poly(ADP-ribose): novel functions for an old molecule, Nat. Rev. Mol. Cell Biol. 7 (7) (2006) 517–528.
[40] W.K. Gruenbaum Y, A. Harel, M. Goldberg, M. Cohen, Review: nuclear lamins–structural proteins with fundamental functions, J. Struct. Biol. 129 (2–3) (2000) 313–323.
[41] M.M.T. Yabuki, Y. Doi, et al., Role of nuclear lamins in nuclear segmentation of human neutrophils, Physiol. Chem. Phys. Med. NMR 31 (2) (1999) 77–84.
[42] K.C.A. Orth, M. Garg, C.J. Froelich, V.M. Dixit, The CED-3/ICE-like protease Mch2 is activated during apoptosis and cleaves the death substrate lamin A, J. Biol. Chem. 271 (28) (1996) 16443–16446.
[43] C.C.L.M. Xue, Y. Zhao, et al., Tumor microenvironment-activatable Fe-doxorubicin preloaded amorphous $CaCO_3$ nanoformulation triggers ferroptosis in target tumor cells, Sci. Adv. 6 (18) (2020) eaax1346.
[44] C.A. Chambers DC, S.W. Lukowski, J.E. Powell, Transcriptomics and single-cell RNA-sequencing, Respirology 24 (1) (2019) 29–36.
[45] C.P. Tian XT, H. Zhang, Y.H. Li, X.B. Yin, GSH-activated MRI-guided enhanced photodynamic- and chemo-combination therapy with a MnO_2-coated porphyrin metal organic framework, Chem. Commun. (Camb). 55 (44) (2019) 6241–6244.
[46] G. Lei, Y. Zhang, P. Koppula, et al., The role of ferroptosis in ionizing radiation-induced cell death and tumor suppression, Cell Res. 30 (2020) 146–162.
[47] V.S.R.M.J. Viswanathan, et al., Dependency of a therapy-resistant state of cancer cells on a lipid peroxidase pathway, Nature 547 (7664) (2017) 453–457.
[48] R.N. Kalyane D, R. Maheshwari, V. Tambe, K. Kalia, R.K. Tekade, Employment of enhanced permeability and retention effect (EPR): nanoparticle-based precision

tools for targeting of therapeutic and diagnostic agent in cancer, Mater. Sci. Eng. C Mater. Biol. Appl. 98 (2019) 1252–1276.
[49] N.J. Rich JT, R.C. Paniello, C.C. Voelker, B. Nussenbaum, E.W. Wang, A practical guide to understanding Kaplan-Meier curves, Otolaryngol. Head Neck Surg. 143 (3) (2010) 331–336.
[50] R.W.R. Yerushalmi, P.M. Ravdin, M.M. Hayes, K.A. Gelmon, Ki67 in breast cancer: prognostic and predictive potential, Lancet Oncol. 11 (2) (2010) 174–183.
[51] L.Q. Zhou, C.H. Dong, L. Ding, W. Feng, L.D. Yu, X.W. Cui, Y. Chen, Targeting ferroptosis synergistically sensitizes apoptotic sonodynamic anti-tumor nanotherapy, Nano Today 39 (2021).